

Flower-like NiFe Oxide Nanosheets on Ni Foam as Efficient Bifunctional Electrocatalysts for the Overall Water Splitting

Bo Li, Qin Feng, Feng Jiang, Lizhi Peng, Tianfu Liu*

School of Chemistry and Chemical Engineering, Beijing Institute of Technology, Beijing, 100081, P. R. China

*E-mail: liutf@bit.edu.cn

Received: 8 December 2018 / Accepted: 11 February 2019 / Published: 10 April 2019

Since the oxygen evolution reaction (OER) is a fundamental step in the overall water splitting process, it is necessary for an ideal catalyst to require a small amount of energy to overcome the energy barrier at the electrode-electrolyte interface. Therefore, developing highly active and integrated catalysts is of great significance. Herein, we present a facile and viable method to fabricate flower-like NiFe oxide nanosheets electrocatalysts that are directly grown on nickel foam substrates through a hydrothermal reaction. By tuning the Ni:Fe ratio, the as-synthesized NiFe oxide exhibits excellent catalytic activity that surpasses the activity of the RuO₂ benchmark catalyst, when tested as an electrocatalyst for the overall water splitting reaction. More importantly, the optimized NiFe oxide electrode possesses excellent OER activity in 1 M KOH with small overpotentials of 255 and 280 mV at 10 and 50 mA cm⁻², respectively. When employed as a stable bifunctional catalyst to split water, this electrode achieved a current density of 10 mA cm⁻² at a cell voltage of 1.59 V. This work presents a highly promising candidate for use as an electrode material and represents promising progress in its practical utilization and comprehensive industrialization.

Keywords: NiFe oxide; oxygen evolution reaction; bifunctional catalyst; electrocatalysts

1. INTRODUCTION

With the growing population and the progression of modern society, the demand for energy is increasing. The depletion of fossil-fuel energy and the greenhouse effect their use causes promote the exploration of sustainable, efficient, and clean energy sources and energy storage, which has become an arduous task to solve.[1-4] Solar energy is one of the most abundant natural resources, inspiring the exploration of appropriate ways to utilize it.[5, 6] The use of light and electricity to split water to obtain hydrogen and oxygen is one of the most promising technologies for converting solar and electrical energy into chemical energy. The oxygen evolution reaction (OER) and the hydrogen evolution reaction

(HER) are the two half reactions, and play critical roles in enhancing the efficiency of the overall reaction. In contrast to the HER, the OER is a kinetically extremely sluggish process involving 4 electron transfer steps, which determines the efficiency of the whole electrolysis process of water.[7, 8] Therefore, the main challenge is to develop robust, durable, and economical OER catalysts at present, which would have broad and unprecedented significance. As excellent catalysts, RuO₂ and IrO₂ have been widely studied, limiting wide application due to exorbitant price and extreme scarcity. [9, 10]

Transition metal catalysts such as Ni,[11, 12] Fe,[13, 14] Co[15, 16] and their derivatives[17-22] can be an effective alternative to precious metals because of their low costs, high availabilities and high activities. Ni-based oxides are often incorporated with other elements as an effective non-noble metal catalyst that can improve the stability of the catalyst,[23, 24] which is a problem in single metal oxides. Dougherty [25] reported a series of transition metal oxide electrolysis catalysts for the OER and demonstrated the NiFe oxide was the optimal catalyst in this group. Li [26] investigated the low overpotential of NiFe(OH)₂ for use as an anode catalyst in alkaline medium. Even though many advances have been made in electrolyzed water catalysts based on NiFe, there are limitations in catalyst activity for commercializing.[27] Further studies have shown that active Ni active species could improve the catalytic performance of the catalyst.[28-31]

Inspired by the previous successes of NiFe oxide electrocatalysts, in this work, we report a facile and viable establishment for producing effective OER catalysts in this work, which exhibits superior activity and sufficient stability under alkaline conditions. The OER catalysts are composed of NiFe oxides, which are grown directly on nickel foam substrates by a hydrothermal reaction. The optimized 0.06 M Fe NiFe oxide (Ni_{0.77}Fe_{0.23}) electrode possesses outstanding OER activity with small overpotentials of 255 and 280 mV at 10 and 50 mA cm⁻², respectively. Although manufacturing the raw materials is inexpensive and simple, the synthesized catalyst reveals an excellent electrocatalytic OER performance that is better than benchmark OER catalyst materials, including the well-known high performance RuO₂ nanoparticles. In particular, the catalyst demonstrates no significant performance decay over 12 h of chronopotentiometry measurement at a current density of 50 mA cm⁻². At the same time, it can be used as a stable bifunctional catalyst to split water, which can reach 10 mA cm⁻² at a cell voltage of 1.59 V. All these evidently indicate the catalyst represents a promising progress in the practical utilization and comprehensive industrialization of NiFe oxides.

2. EXPERIMENTAL

2.1 Synthesis

All chemicals were of analytical grade and used without further purification. Nickel chloride hexahydrate (NiCl₂·6H₂O), urea (CO(NH₂)₂), potassium hydroxide (KOH), and ethanol (CH₃CH₂OH) were purchased from Beijing Chemical Works. Ammonium ferrous sulfate hexahydrate ((NH₄)₂Fe(SO₄)₂·6H₂O) was supplied by Sinopharm Chemical Reagent Co. Ltd. Nickel foam of 1×2 cm in size was obtained from Shenzhen Kejing Star Technology Co. Ltd. Typically, an aqueous solution containing (15 mL) 0.2 mol/L of NiCl₂, certain amounts of (NH₄)₂Fe(SO₄)₂, 1 mol/L of urea and the

pretreated nickel foam were put into a 25 ml capacity Teflon-lined autoclave and heated at 90 °C for 32 h. The synthetic conditions were optimized by adjusting the amount of ammonium ferrous sulfate hexahydrate ((NH₄)₂Fe(SO₄)₂·6H₂O), which varied from 0.005 mol/L to 0.07 mol/L (0.005, 0.01, 0.015, 0.02, 0.025, 0.03, 0.035, 0.04, 0.045, 0.05, 0.055, 0.06, 0.065, and 0.07 mol/L). After cooling to room temperature, the obtained nickel foam coated precipitate was thoroughly washed with ethanol and distilled water for 3 times, subsequently dried in an oven at 80 °C for 2 h and finally calcined at 300 °C for 3 h in air. For comparison, a pretreated nickel foam was also calcined under the same conditions without undergoing the hydrothermal reaction.

2.2 Electrochemical measurements

The electrocatalytic performances of the NiFe oxide catalysts supported on the nickel foam were investigated on a CHI660E electrochemical workstation with a three-electrode system with a 1 M KOH (pH = 14) aqueous solution as the electrolyte, for which the NiFe oxide was used as the working electrode, a graphite rod was used as the counter electrode, and a Ag/AgCl (3.5 M KCl) was used as the reference electrode. The cyclic voltammetry (CV) curves were measured over the potential window of 0 - 0.7 V vs. Ag/AgCl at a scan rate of 20 mV s⁻¹. The linear sweep voltammetry (LSV) curves were obtained at a sweep rate of 1 mV s⁻¹ in the voltage range of 0.35-0.55 V vs. Ag/AgCl. Lastly, the chronoamperometric measurements were obtained under the same experimental setup. The linear sweep voltammetry (LSV) curves of the HER were performed at 5 mV s⁻¹. The linear sweep voltammetry (LSV) of overall water splitting was carried out in a two-electrode system with the 0.06M Fe NiFe oxide acting as both the anode and cathode at a scan rate of 10 mV s⁻¹. The polarization curves were recorded without compensating for the iR drop. All potential measurements were converted to potential vs. RHE based on the equation: $E(\text{RHE}) = E(\text{Ag/AgCl}) + (0.205 + 0.059 \times \text{pH})$.

2.3 Physical Characterizations

Powder X-ray diffraction (XRD) patterns were performed using a Bruker D8 advance diffraction system with a Cu K α source. The reference patterns were matched to the experimental data in the Jade Software. Raman spectroscopy measurements were performed on a Witec alpha 300R confocal Raman microscope using a 1800 line per mm grating and a 532 nm diode laser at an incident power of 4 mW and a spot size of 300 nm. X-ray photoelectron spectroscopy (XPS) was carried out on a Thermo Scientific ESCALAB 250Xi X-ray photoelectron spectrometer. The XPS data were analyzed and fitted with XPSPEAK 4.1 software. The morphology of the samples was imaged by field-emission scanning electron microscope (FESEM) on a Hitachi SU-8000. Transmission electron microscopy (TEM) image was obtained on an FEI Tecnai G2 F20.

3. RESULTS AND DISCUSSION

Typical cyclic voltammetry curves of nickel oxide and NiFe oxides with Fe concentrations equal to 0.01 M, 0.04 M, and 0.06 M are presented in Fig. 1. The wide peak in the anodic sweep of nickel

oxide is at 0.413 V vs Ag/AgCl, which corresponds with the $\text{Ni}^{2+}/\text{Ni}^{3+}$ redox transition. However, the voltammetric behavior of the nickel oxide is notably different from that of fresh nickel foam. This difference is attributed to the fact that the electrochemical properties of the nickel foam are robustly dependent upon the calcination process.[32] From the curves in Fig.1, the main redox peaks are associated with the $\text{Ni}^{2+}/\text{Ni}^{3+}$ transition. Although the peaks are clearly found in the same range, a positive shift in the peak potentials is intuitively observed as the concentration of Fe increases. This result implies that the electrochemical performance of the nickel foam has been modified by the co-loading of Fe into the NiO, which is closely related to the incorporation of Ni and Fe.[33] At the same time, the integrated area of the redox peaks in the anodic sweeps also enhance with increasing Fe concentration, reflecting an increase of the bulk electron transport. The addition of iron effectively increased the affinity for the reaction intermediates and enhanced the kinetic activity.[34] The larger intensities of the anodic peaks imply that the active center is strengthening. The active center is closely associated with the synergistic effects of Ni and Fe, facilitating the catalytic activity of the NiFe oxide.[35]

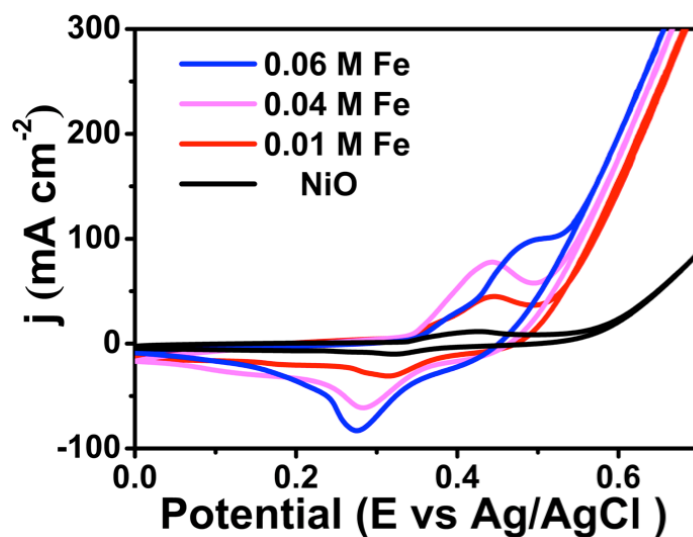


Figure 1. CV plots of the OER process performed on 0.01 M, 0.04 M, and 0.06 M Fe NiFe oxide and nickel oxide electrodes in 1 M KOH with a scan rate of 10 mV s^{-1} .

Therefore, we used the linear sweep voltammetry (LSV) to quantify the changes in the catalytic activity characteristics of NiFe oxide as a function of the Fe composition. The LSV curves of NiO and NiFe oxide of various doping concentrations are recorded in Fig. 2a. As shown in Fig. 2a, the use of NiO as the working electrode in a three-electrode system affords extremely slow dynamics, which has already exceeded the voltage range of the research by the time it reaches 10 mA cm^{-2} . The 0.06 M Fe variant of NiFe oxide reaches 10 mA cm^{-2} at a potential of 1.48 V, compared to a potential of 1.52 V for the 0.04 M and 1.54 V for the 0.01 M. The significant drop of the potential indicates that the OER activity of NiFe oxide enhance with increasing Fe concentration. This indicates that more active sites are exposed and is consistent with the CV results. However, when the concentration of Fe is further increased, the OER activity of the NiFe oxide decreases. The iron sites around nickel are more active and the catalyst

activity is improved. As the iron concentration exceeds a threshold level, a portion of the iron replaces the Ni surface active sites, resulting in less exposed Ni reactions.

Table 1. Comparison of catalyst activity from works published in recent years.

Catalyst	Substrate	Electrolyte	η_{10} (mV)	Tafel Slope (mv dec ⁻¹)	Ref
Fe-NiO _x	Glassy Carbon	1 M KOH	310	49	[36]
NiFe MOF	Nickel Foam	0.1 M KOH	270	47	[37]
NiCoFe LDH	Nickel Foam	0.1 M KOH	275	93	[38]
Ni-NiO CNT	Glassy Carbon	1 M KOH	320	80	[39]
NiFe Oxide	Glassy Carbon	1 M KOH	328	42	[40]
Ni@NC-800	Nickel Foam	1 M KOH	280	45	[41]
NiFe Oxide	Nickel Foam	1 M KOH	255	55	This work

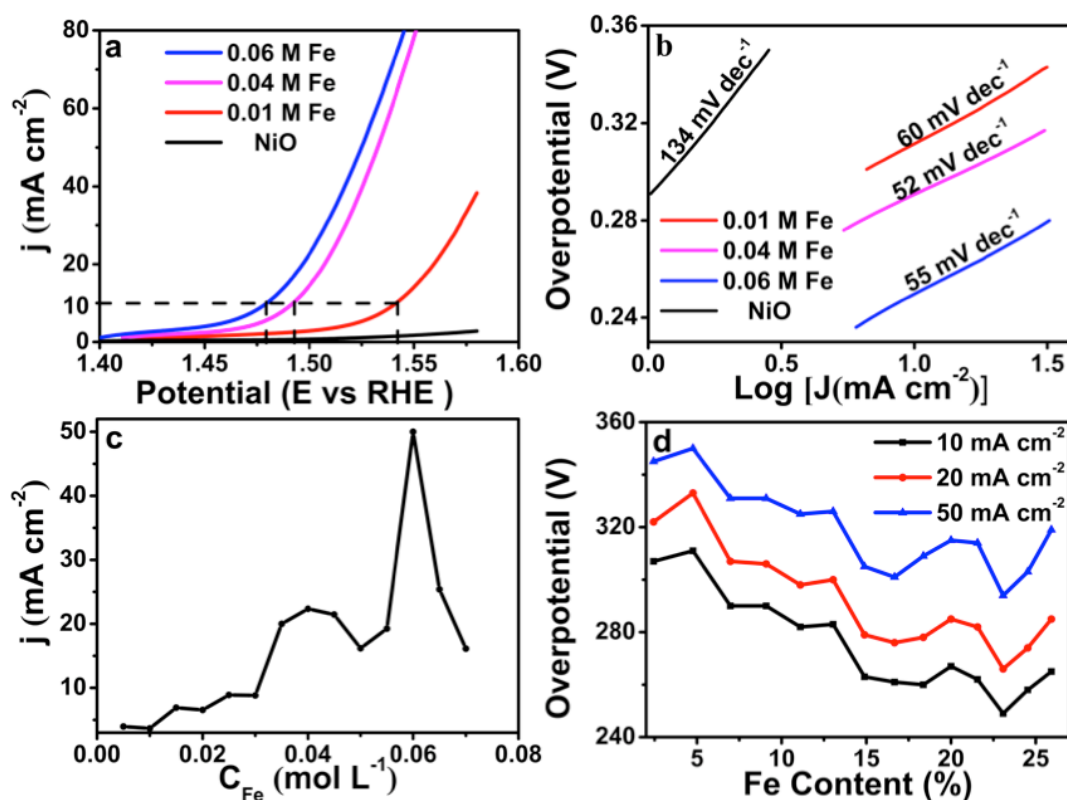


Figure 2. (a) LSV polarization curves for the OER and (b) Tafel plots of the nickel oxide and 0.01 M, 0.04 M, and 0.06 M Fe NiFe oxide with the corresponding Tafel slopes for the OER process. (c) Electrochemical oxygen evolution activity at a fixed overpotential of 280 mV for the NiFe oxides with varying Fe concentrations. (d) Dependence of the overpotentials for the NiFe oxide of varying Fe concentration at 10, 20, 50 mA cm⁻².

The steady-state Tafel measurements for the NiFe oxides are presented in Fig. 2b. Consistent with the LSV results in Fig. 2a, the overpotentials decrease as the Fe content of the NiFe oxides increases. From NiO to the 0.01 M Fe NiFe oxide, the slope drops to half that of the former (from 137 mV dec⁻¹ to 75 mV dec⁻¹), while the slope of the 0.06 M Fe NiFe oxide does not change significantly from that of the 0.02 M Fe sample. Namely, the OER activities of the NiFe oxides do not monotonically increase with enhancing Fe content.[42] And the optimal ratio of Ni_{0.77}Fe_{0.23} represents a significant improvement compared to the previously reported results in Table 1. To further study the effects of Fe content on the OER activity of the NiFe oxides, the current density at a certain overpotential as a function of the Fe content is plotted, as shown in Fig. 2c. This overpotential is selected because it reflects the onset potential of the practical current density. At an overpotential of 280 mV, the catalytic activity tardily changes in the range of 2.4% to 13%, increasing to 8 mA cm⁻² from an initial value of 4 mA cm⁻². Nevertheless, the current density drastically increases at 14.9%, which may be caused by mass transport phenomena, and variations in the electrical conductivity of the different NiFe oxides.[43] The catalytic activity peaks at approximately 23 %, achieving a maximum of 32 mA cm⁻², which is consistent with the results of Landon.[44] As the Fe content increases beyond 23%, the catalytic activity begins to decline. To further explore the influence of the iron content, the overpotentials corresponding to 10, 20 and 50 mA cm⁻² are plotted as a function of the iron content in Fig. 2d. As shown in the curves, a general downward trend from 2.4% to 23% occurs, where the lowest overpotential appears at 23%, coinciding with the composition of NiFe oxide reported by Bell.[34] The changes in the three curves are consistent, indicating that the activity of NiFe oxides grows steadily after 10 mA cm⁻² and the slopes have not deteriorated. The lowest points of 10, 20 and 50 mA cm⁻² correspond to overpotentials of 255, 260 and 280 mV, respectively, which are obviously better than those previously reported for NiFe oxide loaded onto nickel foam. In comparison, RuO₂ at 10 mA cm⁻² corresponded to an overpotential of 380 mV, which is regarded as the benchmark for typical OER catalysts.[45] The Fe dopant modifies the configuration of the NiFe oxides, forms Fe-doped β-NiOOH and decreases the adsorption energy of *OH in NiOOH.[46] NiOOH type is produced by further oxidation and hydration of NiO, changing the formal oxidation state of Ni from +2 to +3. This is reflected by a dramatic weakening of the adsorption energy, such that the activity of the NiFe oxide doped with 23% Fe enhances rapidly.[47]

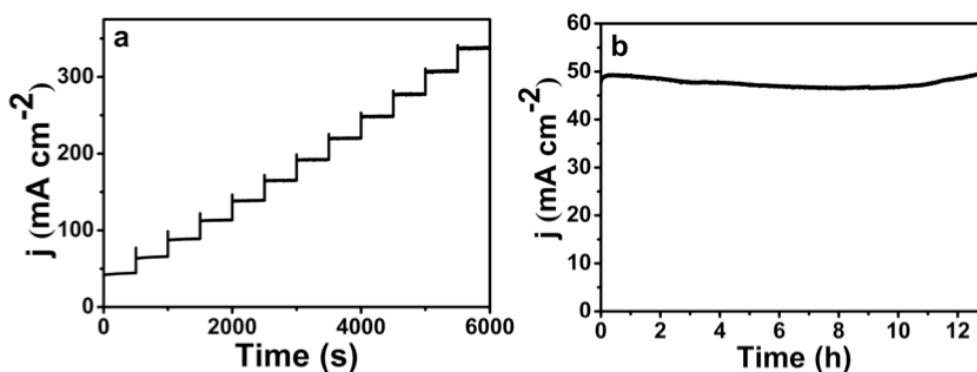


Figure 3. (a) The multi-step chronoamperometric curve of the 0.06 M Fe NiFe oxide without iR correction. (b) The chronoamperometric curve of the 0.06 M Fe NiFe oxide at an overpotential of 280 mV.

Fig. 3a shows the multi-step chronopotentiometric curve of $\text{Ni}_{0.77}\text{Fe}_{0.23}$ in 1 M KOH. From 40 to 340 mA cm^{-2} , the current density increases 27 mA cm^{-2} per 500 s, and the corresponding potential was recorded. At the beginning of the test, the current density stabilizes at 40 mA cm^{-2} and remains stable for the rest 500 s. For the later test results up to 200 mA cm^{-2} , analogical results can be obtained for the various current densities. The chronopotentiometric response implies the outstanding mass transport properties and mechanical robustness of the NiFe oxide electrode for the OER.[48]

To further explore the stability of $\text{Ni}_{0.77}\text{Fe}_{0.23}$, the chronopotentiometric curve is used to investigate the decay of the current density over time, for which the overpotential is fixed at 280 mV. The electrochemical stability of the NiFe oxide electrode is tested in 1 M KOH, as performed in Fig. 3b. The NiFe oxide shows promising durability for 12 h at the fixed overpotential, owing to the activation process of the mass diffusion process between the electrolyte and electrode.[49, 50]

For a more through study of the NiFe oxides, the HER activity of the NiFe oxides is compared with that of NiO under identical conditions. Different Fe contents in the NiFe oxides show different HER activities at 20 mA cm^{-2} , as shown in Fig. 4a, and the NiFe oxide with 0.06 M Fe exhibits the best HER activity with a particularly low overpotential of 193 mV. The NiFe oxide with 0.06 M Fe demonstrates a superior performance compared to that of other materials that have utilized a graphite rod as the counter electrode.[51-53]

Supported by the bifunctional performance of the NiFe oxides for both the HER and OER, the overall water splitting properties of the NiFe oxides are estimated by a two-electrode configuration, which employs the NiFe oxide with 0.06 M Fe as both the anode and cathode. Compared to NiO, which exhibits a cell voltage of 1.85 V in 1 M KOH solution as shown in Fig. 4b, the NiFe oxide of 0.06 M Fe obtains a current density of 10 mA cm^{-2} at a cell voltage of 1.59 V. The activity of the NiFe oxide with 0.06 M Fe is comparable to and even greater than numerous Ni-based catalysts for water splitting that have been reported recently.[54, 55]

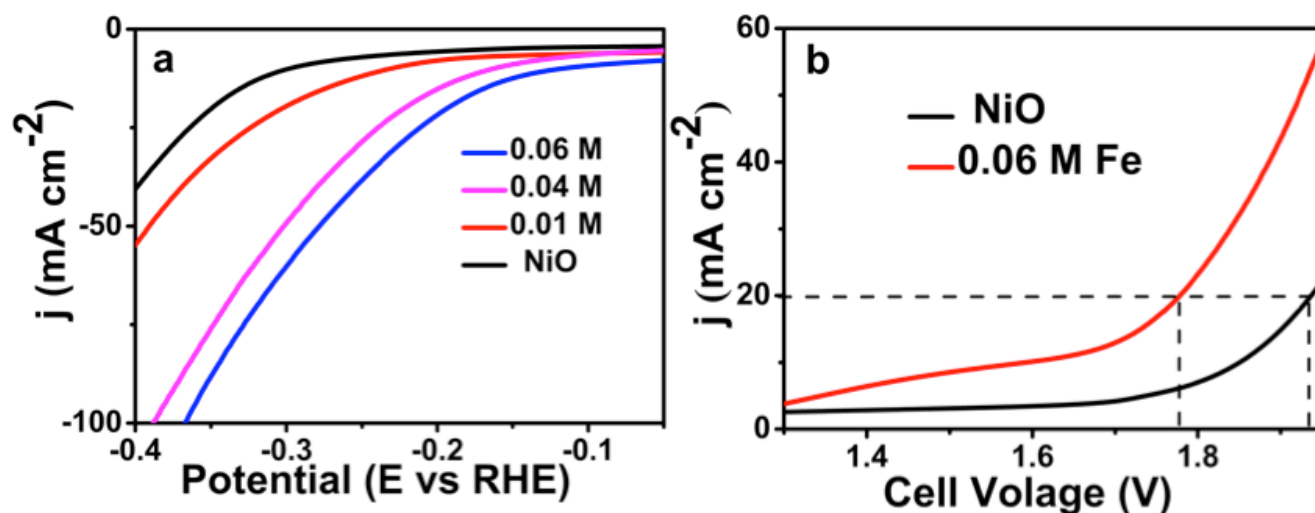


Figure 4. (a) LSV polarization curves toward the HER for nickel oxide and the 0.01 M, 0.04 M and 0.06 M Fe NiFe oxide. (b) LSV polarization curves of the overall water splitting reaction for the 0.06 M Fe NiFe oxide and nickel oxide.

To avoid the influence of the strong peaks of nickel substrate, the NiFe oxides are removed from the nickel foam to analyze their crystal structures.[29] The formation of NiFe oxides is characterized by XRD and the resultant patterns are shown in Fig. 5a. In the scanning range from 20 to 80 degrees, for NiFe oxides, only three weak peaks at 37.3°, 43.3° and 62.9° are exhibited, representing the (111), (200) and (220) facets of NiO, respectively. However, there is no clear evidence for the characteristic peak of Fe, which implies that the Fe atoms have been incorporated into the NiO lattice. As the Fe concentration increases, the peak positions shift to lower 2θ values. This shift demonstrates the success of the Fe doping, which leads to lattice distortion.[43] The lattice constants shift to higher values as the peaks shift, indicating that the Fe ions have been substitutionally incorporated into the NiO structure. The broadening of the characteristic peaks of the NiFe oxides indicates the formation of smaller grains and a poorer crystallinity.

To further characterize the NiFe oxides, Raman spectroscopy was used. In Fig. 5b, it can be seen that there are two peaks at 557 and 666 cm^{-1} . The broad peak at approximately 557 cm^{-1} , corresponding to Ni-O, shifts to higher wavenumbers with Fe doping. The other peak showed the presence of the Fe ions.[56] The anomalously high solubility of Fe in the NiO structure of rock salt can be attributed to the dynamic control of the NiFe oxides formation during the hydrothermal process and the influence of the nanometer scale.[57, 58]

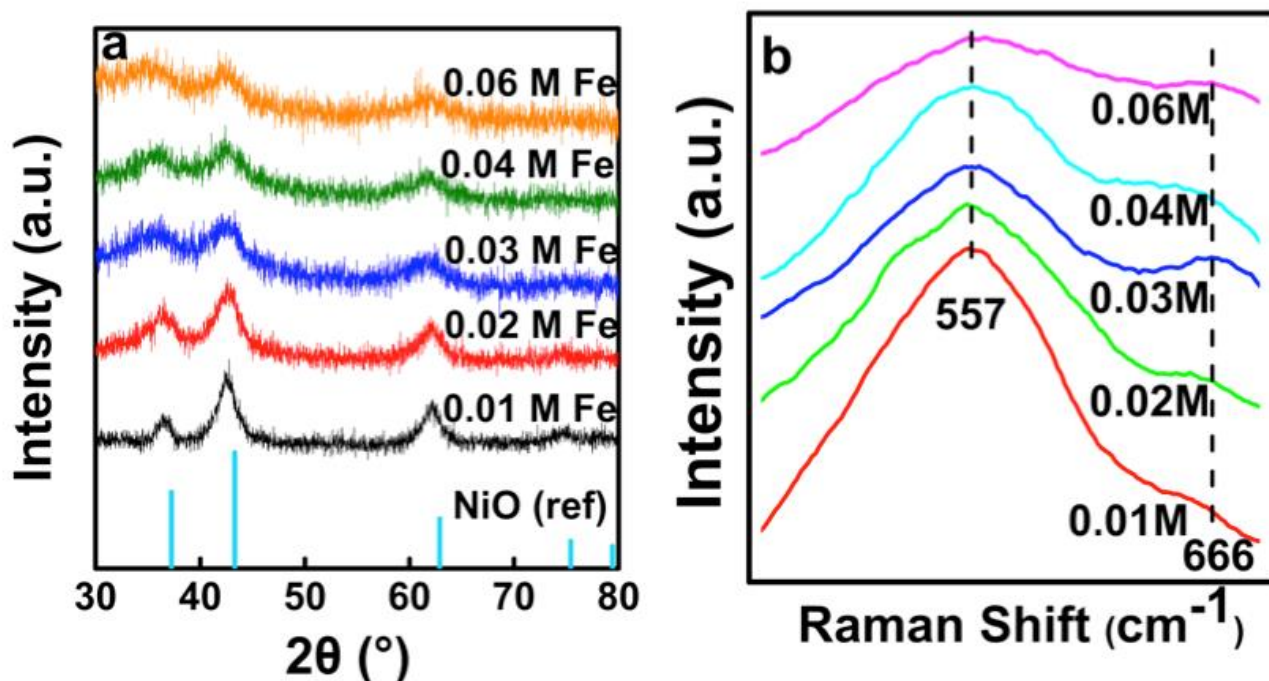


Figure 5. (a) XRD patterns of the NiFe oxide with varying Fe concentrations. (b) Raman spectra of the NiFe oxide with varying Fe concentrations.

From the SEM images in Fig. 6, it can be seen that the particle morphology changes with increasing Fe concentration between 2.4% and 23%. It is thus revealed that doping with Fe atoms can effectively regulate the morphology of the particles. In the preparation process, Fe^{3+} can easily enter the lattice of layered nickel hydroxide, which is then converted into Fe-doped NiO during the later annealing

process. The Fe^{3+} ions replace the surface Ni^{2+} ions and optimize the distribution and variation in the binding energy of the surface oxygen. [59] The corresponding SEM image of $\text{Ni}_{0.77}\text{Fe}_{0.23}$ shows that the surface of the nanosheets is uniformly covered with numerous distributed gaps in Fig. 6c. Hence, it can be expected that a large number of exposed active sites contribute to the water splitting. In Fig. 6d, $\text{Ni}_{0.77}\text{Fe}_{0.23}$ shows adjacent lattice fringes that are 0.22 nm apart, which is slightly larger than the 0.21 nm of the (2 0 0) cubic NiO plane. This result further verifies that as the concentration of Fe enhances, the lattice constants of NiO shift to higher value.

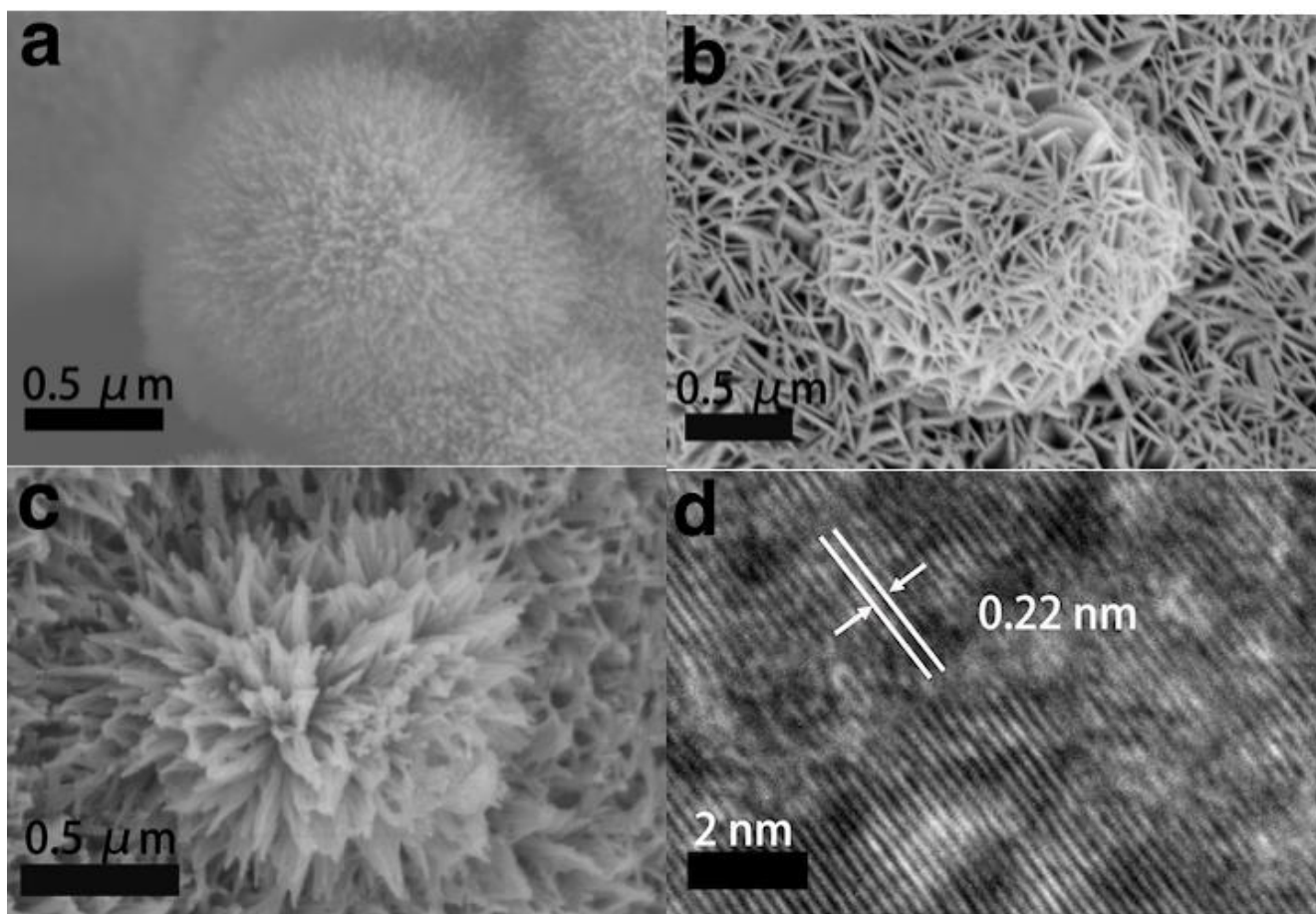


Figure 6. SEM micrographs for the NiFe oxides with (a) 0.01 M, (b) 0.04 M, (c) and 0.06 M Fe. (d) HRTEM image of $\text{Ni}_{0.77}\text{Fe}_{0.23}$.

XPS was employed to detect the surface atomic composition and the chemical shifts in the peaks, and the results are shown in Fig. 7. In Fig. 7a, the survey scans for the NiFe oxides with three Fe concentrations are presented. The Ni 2p core level and the Fe 2p core level are present in the NiFe oxides at 854.9 eV and 711.9 eV, respectively. This indicates that Fe has been doped into the samples during their synthesis. In Fig. 7b, it can be seen that the two main peaks for Ni 2p are located at 854 and 873 eV, corresponding to its $2p_{3/2}$ and $2p_{1/2}$ levels, respectively, and the satellite peaks at 866 and 879 eV are visible. This is consistent with the XPS spectra of NiO that have been reported in the literature,[32, 60, 61] and it proves that Ni^{2+} is the primary form of Ni and no Ni^{3+} is present. Meanwhile, quantifiable chemical shifts in the binding energy are clearly observed for the NiFe oxides with increasing Fe

concentrations. In addition, the size of the nanoparticles might affect the fluctuations in the binding energy,[62] which is related to the reduction of the grain sizes observed in the XRD results. However, the Fe-doped NiO does not influence the shape of the Ni 2p photoelectron line. Similar peaks represent similar oxidation states and chemical environments in the lattice. From the three curves of the NiFe oxides in Fig. 7c, there are two peaks located at 811 and 824 eV, corresponding to the Fe 2p_{3/2} and Fe 2p_{1/2} levels, respectively, which is in accordance with Fe³⁺ in the Fe-O bond.[63, 64] Fe³⁺ is incorporated into the NiO lattice without forming an independent Fe₂O₃ phase, which is confirmed by the absence of shakeup satellites at 719 eV and 732 eV.[44] The intensity of the Fe 2p_{1/2} peak increases gradually, while that of Ni 2p_{1/2} becomes weaker, which is consistent with the increasing Fe doping concentration. Nevertheless, quantitative analysis of the Ni 2p envelope in this case is complex because of the overlap between the Ni 3d and O 2p electrons, resulting in numerous multiplet structures and shakeup satellites. [61]

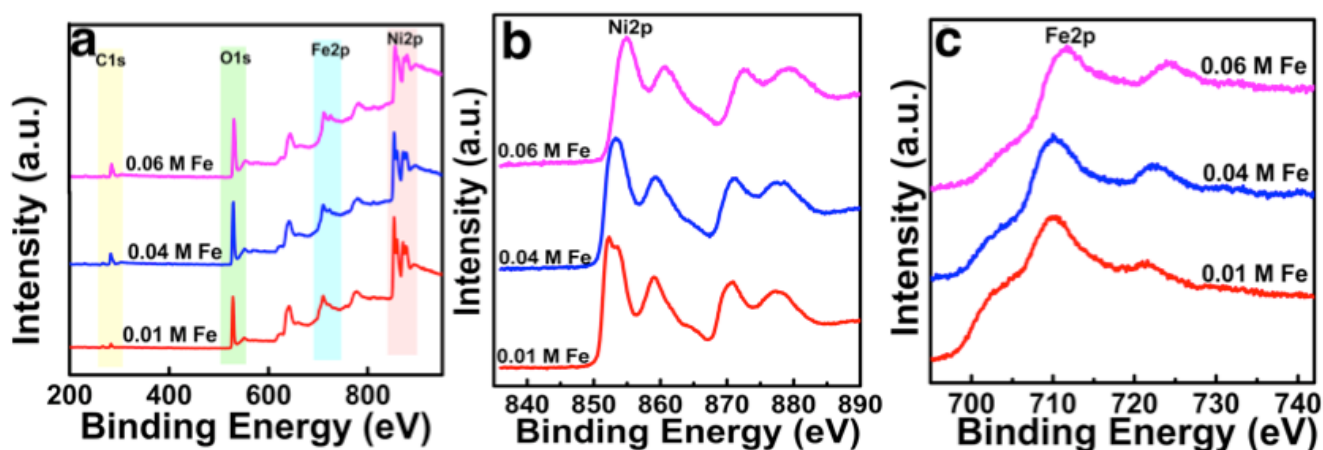


Figure 7. (a) XPS survey spectra for the 0.01 M, 0.04 M and 0.06 M Fe NiFe oxides. (b) High-resolution XPS spectra of the Ni 2p region and (c) Fe 2p region.

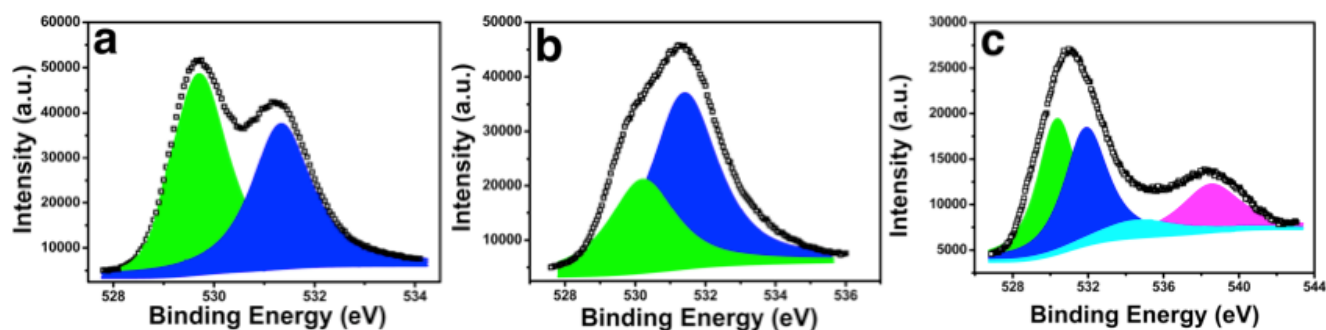


Figure 8. Curve-resolved XPS of the O 1s region for the (a) 0.01 M, (b) 0.04 M, (c) and 0.06 M Fe NiFe oxides.

High resolution scans of the O 1s peak are shown in Fig. 8 and can further reflect the bonding environments of the NiFe oxides surfaces and the degree of hydration. In Fig. 8a and 8b, the spectra show two peaks fit to 529.3 eV (green) and 531 eV (blue) corresponding to the Ni–O and Ni–O–H,

indicating two distinct bonding states of O in the NiFe oxides. However, there are two additional peaks at 533.4 eV (light blue) and 532.5 eV (purple) in Fig. 8c, which are related to the adsorbed O–H and adsorbed H₂O bonding states, respectively. Although the NiFe oxides surface may have formed different states during the synthesis process, the different peaks of the oxides surface may be caused by either incomplete reaction of the precursor materials or the ambient environment.[65] After all, all samples are briefly exposed to air. Hydroxylation is a common phenomenon in oxide materials, and these NiFe oxides are no exception.

4. CONCLUSIONS

In summary, flower-like NiFe oxides nanosheets with different Fe concentrations were successfully loaded onto the nickel foam by hydrothermal reaction and subsequent annealing. The unique flower-like nanosheets architecture offers an abundance of catalytic active sites. More importantly, the addition of iron effectively increases the affinity for the reaction intermediates and enhances the kinetic activity. The optimal sample with 0.06 M Fe can reach 10 mA at an overpotential of 255mV and a low Tafel slope of 55 mV dec⁻¹. The activity of this sample remains steady for 12 h at a constant 280 mV overpotential at density up to 50 mA cm⁻². The NiFe oxides act as bifunctional electrocatalysts to catalyze the overall water splitting reaction, delivering a current density of 10 mA cm⁻² at a cell voltage of 1.59 V in an alkaline medium. This work presents a fabrication strategy, compositional and structural features for improved NiFe oxides water splitting electrocatalyst, which provides a promising progress in the large-scale industrialization.

ACKNOWLEDGEMENTS

We are grateful for financial support from the National Natural Science Foundation of China (NSFC) (grant No. 21571018).

References

1. S. Chu and A. Majumdar, *Nature*, 488 (2012) 294.
2. M.W. Kanan and D.G. Nocera, *Science*, 321 (2008) 1072.
3. Y. Park, K.J. McDonald and K.-S. Choi, *Chem. Soc. Rev.*, 42 (2013) 2321.
4. J. Rosen, G.S. Hutchings and F. Jiao, *J. Am. Chem. Soc.*, 135 (2013) 4516.
5. B. Klahr, S. Gimenez, F. Fabregat-Santiago, J. Bisquert and T.W. Hamann, *J. Am. Chem. Soc.*, 134 (2012) 16693.
6. H. Shi and G. Zhao, *J. Phys. Chem. C*, 118 (2014) 25939.
7. X. Yu, Z. Sun, Z. Yan, B. Xiang, X. Liu and P. Du, *J. Mater. Chem. A*, 2 (2014) 20823.
8. X. Zou, J. Su, R. Silva, A. Goswami, B.R. Sathe and T. Asefa, *Chem. Commun.*, 49 (2013) 7522.
9. Y. Lee, J. Suntivich, K.J. May, E.E. Perry and Y. Shao-Horn, *J. Phys. Chem. Lett.*, 3 (2012) 399.
10. J. Rossmeisl, Z.W. Qu, H. Zhu, G.J. Kroes and J.K. Nørskov, *J. Electroanal. Chem.*, 607 (2007) 83.
11. G. Wu, W. Chen, X. Zheng, D. He, Y. Luo, X. Wang, J. Yang, Y. Wu, W. Yan, Z. Zhuang, X. Hong and Y. Li, *Nano Energy*, 38 (2017) 167.
12. L. Wang, Y. Wu, R. Cao, L. Ren, M. Chen, X. Feng, J. Zhou and B. Wang, *ACS Appl. Mater. Inter.*,

- 8 (2016) 16736.
13. X. Zhu, C. Tang, H. Wang, B. Li, Q. Zhang, C. Li, C. Yang and F. Wei, *J. Mater. Chem. A.*, 4 (2016) 7245.
 14. I. Elizabeth, A.K. Nair, B.P. Singh and S. Gopukumar, *Electrochim. Acta*, 230 (2017) 98.
 15. J. Qi, W. Zhang, R. Xiang, K. Liu, H. Wang, M. Chen, Y. Han and R. Cao, *Adv. Sci.*, 2 (2015) 1500199.
 16. Y. Xu, W. Tu, B. Zhang, S. Yin, Y. Huang, M. Kraft and R. Xu, *Adv. Mater.*, 29 (2017) 1605957.
 17. X.H. Xia, J.P. Tu, J. Zhang, X.L. Wang, W.K. Zhang and H. Huang, *Sol. Energy Mater. Sol. Cells*, 92 (2008) 628.
 18. A.C. Michael E G Lyons, , Patrick O'Brien, Ian Godwin, Richard L Doyle, *Int. J. Electrochem. Sci.*, 7 (2012) 11768.
 19. W.D. Chemelewski, H.C. Lee, J. Lin, A.J. Bard and C.B. Mullins, *J. Am. Chem. Soc.*, 136 (2014) 2843.
 20. M.E. G Lyons and M.P. Brandon, *Int. J. Electrochem. Sci.*, 3 (2008) 1463.
 21. X. Zhou, X. Shen, Z. Xia, Z. Zhang, J. Li, Y. Ma and Y. Qu, *ACS Appl. Mater. Inter.*, 7 (2015) 20322.
 22. S.X. Liu, W.X. Lv, F.Y. Kong and W Wang, *Int. J. Electrochem. Sci.*, 13 (2018) 3843.
 23. Q. Xie, Z. Cai, P. Li, D. Zhou, Y. Bi, X. Xiong, E. Hu, Y. Li, Y. Kuang and X. Sun, *Nano Res.*, 11 (2018) 4524.
 24. Z. Xue, J. Kang, D. Guo, C. Zhu, C. Li, X. Zhang and Y. Chen, *Electrochim. Acta*, 273 (2018) 229.
 25. W.Q. Yang, Y.X. Hua, Q.B. Zhang, H. Lei and C.Y. Xu, *Electrochim. Acta*, 273 (2018) 71.
 26. S. Yin, W. Tu, Y. Sheng, Y. Du, M. Kraft, A. Borgna and R. Xu, *Adv. Mater.*, 30 (2018) 1705106.
 27. X. Zheng, X. Han, H. Liu, J. Chen, D. Fu, J. Wang, C. Zhong, Y. Deng and W. Hu, *ACS Appl. Mater. Inter.*, 10 (2018) 13675.
 28. J.J. Xuan and Z.W. Liu, *Int. J. Electrochem. Sci.*, 12 (2017) 10471.
 29. L. Trotochaud, S.L. Young, J.K. Ranney and S.W. Boettcher, *J. Am. Chem. Soc.*, 136 (2014) 6744.
 30. I.M. Al-Akraa, Y.M. Asal and S.D. Khamis, *Int. J. Electrochem. Sci.*, 13 (2018) 9712.
 31. M.D. Merrill and R.C. Dougherty, *J. Phys. Chem. C*, 112 (2008) 3655.
 32. X. Li, F.C. Walsh and D. Pletcher, *Phys. Chem. Chem. Phys.*, 13 (2011) 1162.
 33. L. Han, S. Dong and E. Wang, *Adv. Mater.*, 28 (2016) 9266.
 34. M.W. Louie and A.T. Bell, *J. Am. Chem. Soc.*, 135 (2013) 12329.
 35. J. Zhao, X. Ren, Q. Han, D. Fan, X. Sun, X. Kuang, Q. Wei and D. Wu, *Chem. Commun.*, 54 (2018) 4987.
 36. C. Hsu, N. Suen, Y. Hsu, H. Lin, C. Tung, Y. Liao, T. Chan, H. Sheu, S. Chen and H. Chen, *Phys. Chem. Chem. Phys.*, 19 (2017) 8681.
 37. N. Suen, S. Hung, Q. Quan, N. Zhang, Y. Xu and H. Chen, *Chem. Soc. Rev.*, 46 (2017) 337.
 38. M.P. Browne, J.M. Vasconcelos, J. Coelho, M. O'Brien, A.A. Rovetta, E.K. McCarthy, H. Nolan, G.S. Duesberg, V. Nicolosi, P.E. Colavita and M.E.G. Lyons, *Sustainable Energy Fuels*, 1 (2017) 207.
 39. C.H. TenChin Wen, YatJune Li, *J. Electrochem. Soc.*, 140 (1993) 2554.
 40. D. Friebel, M.W. Louie, M. Bajdich, K.E. Sanwald, Y. Cai, A.M. Wise, M.-J. Cheng, D. Sokaras, T.C. Weng, R. AlonsoMori, R.C. Davis, J.R. Bargar, J.K. Nørskov, A. Nilsson and A.T. Bell, *J. Am. Chem. Soc.*, 137 (2015) 1305.
 41. C. Hu and Y. Wu, *Mater. Chem. Phys.*, 82 (2003) 588.
 42. Z. Lu, W. Xu, W. Zhu, Q. Yang, X. Lei, J. Liu, Y. Li, X. Sun and X. Duan, *Chem. Commun.*, 50 (2014) 6479.
 43. A.C. Pebley, E. Decolvenaere, T.M. Pollock and M.J. Gordon, *Nanoscale*, 9 (2017) 15070.
 44. J. Landon, E. Demeter, N. İnoğlu, C. Keturakis, I.E. Wachs, R. Vasić, A.I. Frenkel and J.R. Kitchin, *ACS Catal.*, 2 (2012) 1793.
 45. D. Friebel, M.W. Louie, M. Bajdich, K.E. Sanwald, Y. Cai, A.M. Wise, M.J. Cheng, D. Sokaras,

- T.C. Weng, R. Alonso-Mori, R.C. Davis, J.R. Bargar, J.K. Norskov, A. Nilsson and A.T. Bell, *J. Am. Chem. Soc.*, 137 (2015) 1305.
46. S. Jung, C.C.L. McCrory, I.M. Ferrer, J.C. Peters and T.F. Jaramillo, *J. Mater. Chem. A*, 4 (2016) 3068.
47. O. DiazMorales, I. Ledezma-Yanez, M.T.M. Koper and F. CalleVallejo, *ACS Catal.*, 5 (2015) 5380.
48. Y. Li and A. Selloni, *ACS Catal.*, 4 (2014) 1148.
49. Z. Wu, Z. Zou, J. Huang and F. Gao, *J. Catal.*, 358 (2018) 243.
50. J. Wang, L. Gan, W. Zhang, Y. Peng, H. Yu, Q. Yan, X. Xia and X. Wang, *Sci. Adv.*, 4 (2018) 1.
51. X. Lu and C. Zhao, *Nat. Commun.*, 6 (2015) 6616.
52. K. Ojha, S. Banerjee and A.K. Ganguli, *J. Am. Chem. Soc.*, 129 (2017) 989.
53. K. Qu, Y. Zheng, X. Zhang, K. Davey, S. Dai and S.Z. Qiao, *ACS Nano*, 11 (2017) 7293.
54. Y. Zheng, Y. Jiao, Y. Zhu, L.H. Li, Y. Han, Y. Chen, A. Du, M. Jaroniec and S.Z. Qiao, *Nat. Commun.*, 5 (2014) 3783.
55. C. Shu, S. Kang, Y. Jin, X. Yue and P.K. Shen, *J. Mater. Chem. A*, 5 (2017) 9655.
56. A. Kumar and S. Bhattacharyya, *ACS Appl. Mater. Inter.*, 9 (2017) 41906.
57. J. Zhao, X. Ren, Q. Han, D. Fan, X. Sun, X. Kuang, Q. Wei and D. Wu, *Chem. Commun.*, 54 (2018) 4987.
58. Z. Chen, L. Cai, X. Yang, C. Kronawitter, L. Guo, S. Shen and B.E. Koel, *ACS Catal.*, 8 (2018) 1238.
59. K. Fominykh, P. Chernev, I. Zaharieva, J. Sicklinger, G. Stefanic, M. Döblinger, A. Müller, A. Pokharel, S. Böcklein, C. Scheu, T. Bein and D. Fattakhova-Rohlfing, *ACS Nano*, 9 (2015) 5180.
60. M.N. Iliev, D. Mazumdar, J.X. Ma, A. Gupta, F. Rigato and J. Fontcuberta, *Phys. Rev. B*, 83 (2011) 014108.
61. X. Wu and K. Scott, *Int. J. Hydrogen Energy*, 38 (2013) 3123.
62. H. Ali-Löyty, M.W. Louie, M.R. Singh, L. Li, H.G. Sanchez Casalongue, H. Ogasawara, E.J. Crumlin, Z. Liu, A.T. Bell, A. Nilsson and D. Friebel, *J. Phys. Chem. C*, 120 (2016) 2247.
63. A.P. Grosvenor, M.C. Biesinger, R.S.C. Smart and N.S. McIntyre, *Surf. Sci.*, 600 (2006) 1771.
64. M.A. Peck and M.A. Langell, *Chem. Mater.*, 24 (2012) 4483.
65. A.P. Grosvenor, B.A. Kobe, M.C. Biesinger and N.S. McIntyre, *Surf. Interface. Anal.*, 36 (2004) 1564.
66. G. Liu, X. Gao, K. Wang, D. He and J. Li, *Nano Res.*, 10 (2017) 2096.
67. A.P. Grosvenor, B.A. Kobe and N.S. McIntyre, *Surf. Interface. Anal.*, 36 (2004) 1637.